Journal of Membrane Science 757 (2026) 125992

Contents lists available at ScienceDirect

Journal of Membrane Science

journal homepage: www.elsevier.com/locate/memsci

Multi-criteria evaluation of graphene oxide nanofiltration membranes for decaffeination

Yihan Tian [a], Tongxi Lin [a,*], Yuta Nishina [b], Xiaojun Ren [a,**], Rakesh Joshi [a,***]

[a] School of Materials Science and Engineering, University of New South Wales, Sydney, NSW, 2052, Australia
[b] Research Institute for Interdisciplinary Science, Okayama University, Kita-ku, Okayama, 700-8530, Japan

ARTICLE INFO

Keywords:
Multi-criteria evaluation
Decaffeination
Graphene oxide

ABSTRACT

Nanofiltration (NF) offers a promising low-energy approach for producing decaffeinated instant coffee, while requires membranes that balance caffeine removal, water permeance, and retention of key coffee matrix compounds. Here, graphene oxide membranes (GOMs) were modified by sodium alginate (SA) intercalation, Ca^{2+} crosslinking, and their combined strategy to tune nanochannel structure and separation performance. The results show that membrane modification does not follow a simple monotonic trend; instead, small structural and chemical changes generate competing effects on permeance and selectivity through coupled transport, adsorption, and confinement mechanisms. To identify the most suitable membrane, a multi-criteria evaluation framework (MCEF) combining entropy weighting and TOPSIS was established using five key performance indicators: caffeine removal, flavour-related marker retention index, choline retention, water permeance, and concentration increase. This framework identified CGSM-1 as the best-performing flat membrane, which also showed promising performance in hollow-fibre form. In coffee filtration tests, CGSM-1 reduced caffeine concentration from 24.64 to 12.95 μg/mg, corresponding to a 47.4% reduction, while retaining measurable levels of HMF, trigonelline, NMP, and choline. These findings demonstrate the potential of engineered GOMs for selective caffeine reduction in coffee liquor and provide a practical evaluation strategy for membrane-based decaffeination.

1. Introduction

Decaffeinated coffee has attracted market attention as many consumers seek to limit their daily caffeine intake while still enjoying coffee. The decaffeination process aims to remove caffeine from coffee while retaining as many flavour compounds as possible. Recent decaffeination mainly focuses on treating unroasted green coffee beans, using organic solvent extraction, supercritical carbon dioxide extraction, or water extraction [1]. Although these methods are mature, they may involve organic solvents, high-pressure operation, long processing times, or high energy consumption [2]. Nanofiltration is a highly promising separation technique for decaffeination, yet its potential has not been extensively explored [3–5]. The industrial production of instant coffee typically involves water extraction and drying [1,6]. Therefore, applying nanofiltration directly to extracted coffee liquor may provide a mild and solvent-free route for caffeine reduction [7,8]. In this context, the practical value of membrane-based decaffeination should be considered not only from separation performance, but also from its treated stream, operating condition, solvent use and process burden compared with established decaffeination methods [9,10].

In general, coffee liquor is a complex liquid mixture containing many molecules with varying sizes, molecular weights and charges. Precisely identifying and separating caffeine from this mixture while retaining as many other compounds as possible is challenging and therefore places high demands on the selectivity and tunability of membranes. Graphene oxide (GO) laminar membranes are superior next-generation nanofiltration (NF) membranes for precise molecular sieving [11–13]. GO is a hydrophilic two-dimensional (2D) material with abundant oxygen functional groups decorated on the graphene backbone. Through layer stacking, a graphene oxide membrane (GOM) can be fabricated, in which well-defined, ordered interlayer spacing between GO laminates serves as 2D nanochannels for selective mass transport [14–16]. These

* Corresponding author.
** Corresponding author.
*** Corresponding author.
E-mail addresses: tongxi.lin@unsw.edu.au (T. Lin), xiaojun.ren@unsw.edu.au (X. Ren), r.joshi@unsw.edu.au (R. Joshi).

https://doi.org/10.1016/j.memsci.2026.125992
Received 17 May 2026; Received in revised form 10 July 2026; Accepted 2 August 2026
Available online 4 August 2026

nanochannels with sub-nanometre-scale dimensions enable various mechanisms for molecular sieving, including size exclusion and the Donnan effect. Moreover, the functional groups on the GO surface enable high chemical tunability of the nanochannels, allowing multiple effective modification strategies, such as cation crosslinking and polymer intercalation [17–24].

Although interlayer engineering of GO membranes has been widely investigated for ion and molecule separation, most previous studies have focused on water purification, desalination, organic solvent nanofiltration, or single-solute model systems. In contrast, membrane-based decaffeination requires selective caffeine transport in a complex coffee matrix containing chemically similar compounds. This creates a different separation requirement from conventional nanofiltration, where the permeate is usually collected as the purified product. In the present work, caffeine is designed to preferentially permeate through the membrane, while key coffee matrix compounds are retained in the feed, thereby converting the feed solution into a decaffeinated coffee product. This reversed product-collection strategy requires balanced membrane performance rather than simply maximising rejection.

In this work, we systematically investigate the influence of membrane parameters on the decaffeination performance. We fabricated a series of GO-based NF membranes [25], including GOM, Ca^{2+}-crosslinked GOM (CGM), sodium alginate-intercalated GOMs (GSMs) and Ca-crosslinked sodium alginate-intercalated GOMs (CGSMs) and examined their decaffeination performance. Unlike conventional NF processes, where the permeate is usually collected as the purified product, our membranes allow caffeine to pass into the permeate while retaining the coffee matrix compounds in the feed, thereby transforming the feed into a decaffeinated coffee solution. We applied various characterisation techniques to analyse the chemical composition, surface charge, and nanochannel size of the membranes, and to elucidate the structure-performance relationship. To avoid relying on a single performance indicator, we established a multi-criteria evaluation framework that combines the entropy weighting (MCEF) method and the TOPSIS (Technique for Order of Preference by Similarity to Ideal Solution) model to evaluate membrane performance more comprehensively using caffeine removal, flavour-related marker retention, choline retention, water permeance, and concentration increase as key criteria. We further extended our membranes from flat membranes to hollow-fibre membranes to verify their consistency, robustness, and scale-up potential for future large-scale, real-world industrial production and decaffeination.

2. Methods

2.1. Materials

We used commercial freeze-dried instant coffee granules (Moccona Classic, medium roast, strength 5, Jacobs Douwe Egberts, Netherlands). Caffeine, calcium chloride ($CaCl_2$) and sodium alginate (SA) were purchased from Merck Millipore Ltd. Graphene oxide (GO) stock suspension (1.5 wt%, 500 nm flake size) was supplied by NiSiNa Materials Japan. Polyvinylidene fluoride (PVDF) substrate membranes (200 nm pore size, 47 mm diameter) were purchased from the Sterlitech Co. Analytical standard caffeine (≥99% purity) and sodium acetate trihydrate (SAT, 99.86% purity) used in quantitative nuclear magnetic resonance (qNMR) measurements were provided by UNSW NMR Facility. Deuterium oxide (D_2O, ≥99.9 atomic% D) was obtained from Cambridge Isotope Laboratories, Inc.

2.2. Preparation of GO-based membranes

The GO stock suspension was first diluted to 0.5 mg/ml with deionised (DI) water. Then 1 ml of diluted GO suspension was added in 50 ml of DI water, followed by 10 min of ultrasonication. GO is deposited on the substrate membrane to prepare GOM via vacuum filtration. The Ca^2-crosslinked GO membranes (CGMs) were prepared by soaking as prepared GOMs in $CaCl_2$ solution (0.5 M) for 4 h, followed by drying in air. For the preparation of SA-intercalated GO membranes (GSMs). First, 1 ml of GO diluted suspension was mixed with 100 μl (GSM-1), 200 μl (GSM-2), 300 μl (GSM-3), and 400 μl (GSM-4) of SA solution (0.5 mg/ml) and diluted to 50 ml with DI water, respectively. After 4 h of agitation, the mixture was filtered on substrate membrane. Ca^{2+}-crosslinked sodium alginate-intercalated GOMs (CGSMs) were prepared by soaking GSMs in $CaCl_2$ solutions (0.5 M) for 4 h. They were then dried and denoted as CGSM-1, CGSM-2, CGSM-3 and CGSM-4 respectively, according to the addition amount of SA.

The preparation of GO-based hollow fibre (HF) membranes was performed by vacuum filtration. One hollow fibre setup consists of 23 PVDF hollow fibres with an effective area of 0.00629 m^2. For the preparation of GO hollow fibre membrane (HF-GOM), 5 mL of GO stock solution (0.5 mg/ml) was diluted to 250 ml with DI water. After 10 min of ultrasonication at room temperature, the GO solution was added to the hollow fibre setup and filtered under ~0.9 bar pressure. For the preparation of CGSM-1 hollow fibre membrane (HF-CGSM-1). First, 5 ml of GO stock solution was mixed with 500 μl of SA solution (0.5 mg/ml) and then diluted to 250 ml with DI water for 4 h of agitation. The mixture was filtered on PVDF hollow fibres, then soaked in $CaCl_2$ solution (0.5 M) for 4h.

2.3. Membrane characterizations

The morphology of the membranes was observed by field-emission scanning electron microscopy (FE-SEM, FEI Nova NanoSEM 450), and the elemental mapping was obtained by energy-dispersive X-ray spectroscopy (EDS). The lateral-size-related distribution of GO nanosheets was evaluated by dynamic light scattering (DLS) using Malvern Zetasizer Ultra. The hydrophilicity of the membrane surface was evaluated by the Ossila contact angle goniometer. The chemical composition of the membranes was analyzed by the X-ray photoelectron spectroscopy (XPS) and the Fourier transform infrared spectroscopy (FT-IR, PerkinElmer Spectrum Two spectrometer) under the universal attenuated total reflectance (ATR) mode. The X-ray diffraction (PANalytical Empyrean IV Thin-Film XRD) was used to analyse the membrane physical structure at 45 kV 40 mA with Cu Kα radiation ($\lambda = 0.154$ nm). Zeta potential of membrane was determined by streaming potential measurements using a SurPASS electrokinetic analyzer (Anton Paar GmbH, Austria).

2.4. Membrane transport performance

Membrane performance was evaluated via vacuum filtration at room temperature. The effective membrane surface area is 12.57 cm^2. During membrane performance evaluation, 100 ml of coffee solution (1 mg/ml) was used as feed solution. After 24 h of membrane filtration, the retention was collected, and the volumes were measured for coffee permeance calculation. The collected retention was then freeze-dried. The freeze-dried coffee sample was weighed to determine the residual coffee solid mass and therefore the concentration can be calculated, and the enrichment of the membrane process can be evaluated. Experiments were repeated three times to verify reliability and reproducibility. The long-term performance of the membrane was investigated using a vacuum-filtration-based hollow-fibre (HF) setup, similar to that used in our previous studies [25–27]. This filtration experiment was operated in semi-batch mode to simulate continuous industrial operation using 1 mg/ml coffee solution. Fresh feed was continuously added using a peristaltic pump to maintain a constant system volume (60 ml), while the feed solution was periodically refreshed every 24 h. Retention was collected at 24 h intervals (24, 48, 72, and 96 h). The digital photographs of the membranes and the filtration set ups are shown in the **supplementary note. 1**.

The water permeance during coffee filtration is calculated using the

following equation,

$$J = \frac{V_f - V_r}{AP\Delta t} \quad (1)$$

J is the water permeance during filtration, expressed in L m^{-2} h^{-1} bar^{-1} (LMH/bar). V_f is the volume of the feed solution (L). V_r is the volume of the retentate (L). A is the effective membrane surface area, which is 0.001257 m2 for a flat membrane and 0.00629 m^2 for a hollow fibre membrane. P and Δt are the applied pressure (bar) and the filtration time (h), respectively.

The treated coffee concentration was calculated as in equation (2), and the concentration increase is calculated according to equation (3).

$$C_t = \frac{m_d}{V_r} \quad (2)$$

$$\Delta C = \frac{C_t - C_f}{C_f} \cdot 100\% \quad (3)$$

C_t is treated with coffee concentration (mg/ml). m_d is the mass of dried residue. V_r is the volume of the retention solution. ΔC the concentration increase rate (%). C_f is the concentration of feed solution (mg/ml).

2.5. Quantitative determination of flavour compounds in coffee

The quantitative determination of flavour compounds in coffee was performed based on ^{1}H qNMR [28,29]. For each measurement, 10 mg of freeze-dried coffee powders were dispersed in 800 μl of D_2O containing 0.03% w/v sodium acetate trihydrate as an internal standard. Subsequently, the samples were ultrasonicated for 30 min, and then centrifuged at 6000 rpm for 10 min. The supernatant was collected for NMR measurement.

The qNMR measurements were performed by a 400 MHz Bruker Avance III HD NMR system fitted with a Prodigy CryoProbe. A spectral width of 15.98 ppm was applied. For each spectrum, 8 scans are accumulated. The acquisition time was 5.12 s. The relaxation delay (D1) exceeded the longest longitudinal relaxation time of the analytical nucleus (D1 > 5T1max) by 5 times and was set to 60 s to ensure complete relaxation and accurate quantification [30,31]. All experiments were performed at a controlled temperature of 298 K.

2.6. Coffee compound quantification and separation performance

The ^{1}H NMR spectrum of coffee samples is shown in Fig. 1. Bruker Topspin software was used for the data process and analysis. The spectra were treated with exponential apodization in Bruker TopSpin using a line-broadening factor of 0.1 Hz before Fourier transformation to 128K real points. This was followed by phase correction for pure absorption, as well as baseline correction. Subsequently, the signal peaks of each compound were identified and integrated by the comparison of references and caffeine standard [28,29,32]. In this work, the qNMR analysis was focused on caffeine and four representative coffee matrix compounds with distinguishable and well-resolved proton signals, including 5-hydroxymethylfurfural, trigonelline, N-methylpyridinium, and choline. These compounds were selected because they are closely related to coffee roasting, thermal transformation, and coffee matrix composition, and their independent NMR peaks enable reliable quantification.

It should be noted that tannic acid or total polyphenol removal was not quantified in this work. The main phenolic compounds in coffee are chlorogenic acid and its derivatives rather than tannic acid as a single defined model compound. In addition, commercial tannic acid is compositionally heterogeneous, and polyphenols generally show complex and overlapping ^{1}H NMR signals in the coffee matrix, which makes accurate quantification difficult without a dedicated analytical method. Therefore, the qNMR results in this study are used to evaluate caffeine separation and the retention trend of selected non-caffeine coffee markers, however should not be interpreted as a direct measurement of tannic acid or total polyphenol retention.

The mass of each compound was calculated according to equation (4), and the concentration of each compound in the freeze-dried coffee sample was calculated by equation (5).

$$m_{i,n} = \left(\frac{I_{i,n} \cdot N_0}{I_0 \cdot N_{i,n}}\right) \cdot \left(\frac{m_0 \cdot P_0}{M_0}\right) \cdot M_{i,n} \quad (4)$$

$$C_{i,n} = \frac{m_{i,n}}{m_{cof}} \cdot 1000 \quad (5)$$

$m_{i,n}$ is the mass of the compounds (mg). $I_{i,n}$ and I_0 represent the integral area of the compound and the internal standard, respectively. $N_{i,n}$ and N_0 represent the number of protons of the compound and the internal

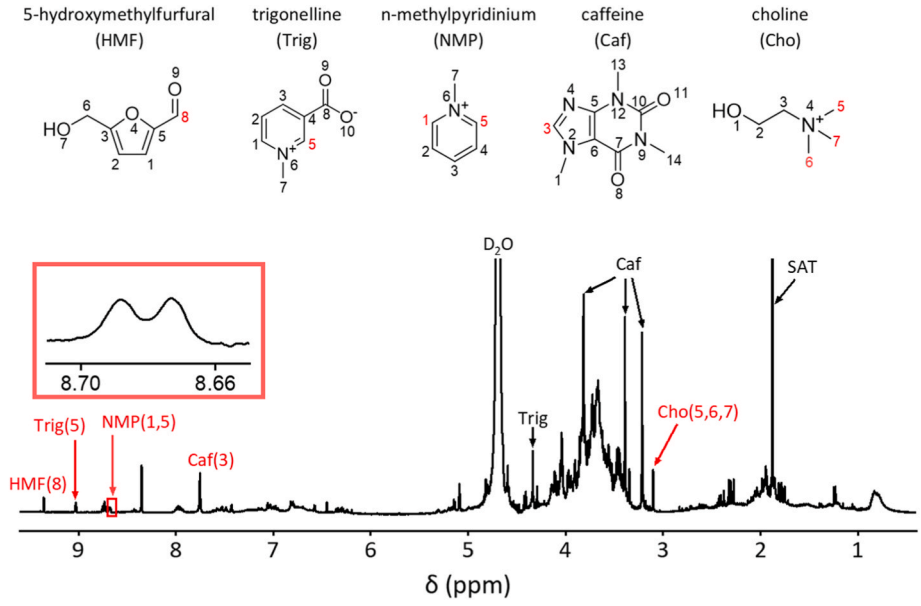

Fig. 1. ^{1}H NMR spectrum of coffee sample. The characteristic peaks corresponding to a specific hydrogen atom in a determined molecule are marked as red, and the marked peaks are used for qNMR determination. The inset with red frame is the magnified spectrum of NMP (1,5) peaks.

standard, respectively. m_0 represents the mass of the internal standard (mg). It is the product of the concentration of the internal standard and the volume of the deuterated reagent used. P_0 is the purity of the internal standard. M_0 is the molar mass of the internal standard (g/mol), and $M_{i,n}$ is the molar mass of the tested compound (g/mol). $C_{i,n}$ is the concentration of each compound in the freeze-dried coffee sample (μg/mg), and m_{cof} is the mass of the corresponding coffee sample (mg). It should be noted that, the subscript i represents the abbreviation of different compounds (Caf for caffeine; Trig for trigonelline; HMF for 5-hydroxymethylfurfural; NMP for n-methylpyridinium and Cho for choline), while n denotes the sample state. $n = f$ and $n = t$ represents the feed and treated samples, respectively.

The caffeine removal (*Rem*, unit in %) after 24h of membrane treatment was calculated as:

$$Rem = \frac{C_{Caf.f} - C_{Caf.t}}{C_{Caf.f}} \cdot 100\% \quad (6)$$

The other compound retentions (R_i, unit in %) after 24 h of filtration were calculated as:

$$R_i = \frac{C_{i.t}}{C_{i.f}} \cdot 100\% \quad (7)$$

3. Results and discussion

3.1. GO-based membranes for decaffeination

The schematic illustration of the fabrication of Ca^{2+}-crosslinked SA-intercalated GOM (CGSM) is shown in Fig. 2a. GO was first mixed with SA in a dispersion and followed by vacuum filtration. The prepared GO-SA membrane was then soaked in a $CaCl_2$ solution for crosslinking. The highly hydrophilic SA polymer matrix is intercalated not only to improve the hydrophilicity of the membranes but also to tune the interlayer spacing of the GO laminates, thereby enhancing water permeance while maintaining caffeine selectivity. Ca ions can facilitate cross-linking both within the SA polymer matrix and across the GO-SA interface. The introduction of Ca ions is intended to increase membrane stability and tune the charge of the nanochannels in the membranes.

The cross-sectional morphology of GOM and CGSM was observed via SEM. GOM demonstrates a typical laminated morphology (Fig. 2b). In contrast, CGSM-1 shows a denser cross-section with fewer laminated features (Fig. 2c), indicating that the GO-SA membrane becomes more compact after Ca-crosslinking. The presence of Ca ions in CGSM-1 is further confirmed via SEM-EDS (Fig. 2d). The surface morphology of the membranes was further analyzed as discussed in the **Supplementary Note. 2 (**Fig. S2**).** The results show that Ca^{2+} crosslinking and SA intercalation reduce surface wrinkles and smooth the membrane surface. In addition to chemical modification, the lateral size of GO nanosheets is also an important structural parameter since it can influence membrane stacking, interflake boundaries, tortuosity, and interlayer transport pathways [33]. The GO nanosheets used in this work show an average size of approximately 600 nm according to DLS analysis (**Supplementary Note. 3,** Fig. S3). Since the same GO source was used for all membranes, the performance differences among GOM, CGM, GSMs and CGSMs are mainly attributed to SA intercalation, Ca^{2+} crosslinking, and their combined effects rather than differences in GO nanosheet size.

3.2. Characterizations of GO-based membranes

The surface hydrophilicity of GOM and the modified GO-based membranes was examined using contact angle measurements (Fig. 3a). The detailed results are summarized in Table S2 in Supplementary Note 3. GOM shows a contact angle of 44.2°, which increases to 50.6° after Ca-crosslinking (CGM). This increase can be attributed to the interaction between Ca ions and oxygen-containing functional groups, which consumes some hydrophilic groups and slightly reduces hydrophilicity. SA is a highly hydrophilic polymer with a contact angle of 34.8° [34,35]. After Ca-crosslinking, the contact angle of Ca-SA decreases to 25.4° (Table S1). The contact angles of CGSMs gradually increase from 38.3° for CGSM-1 to 50.8° for CGSM-4. For CGSM-1 and CGSM-2, because of the low SA content, Ca ions mainly help disperse

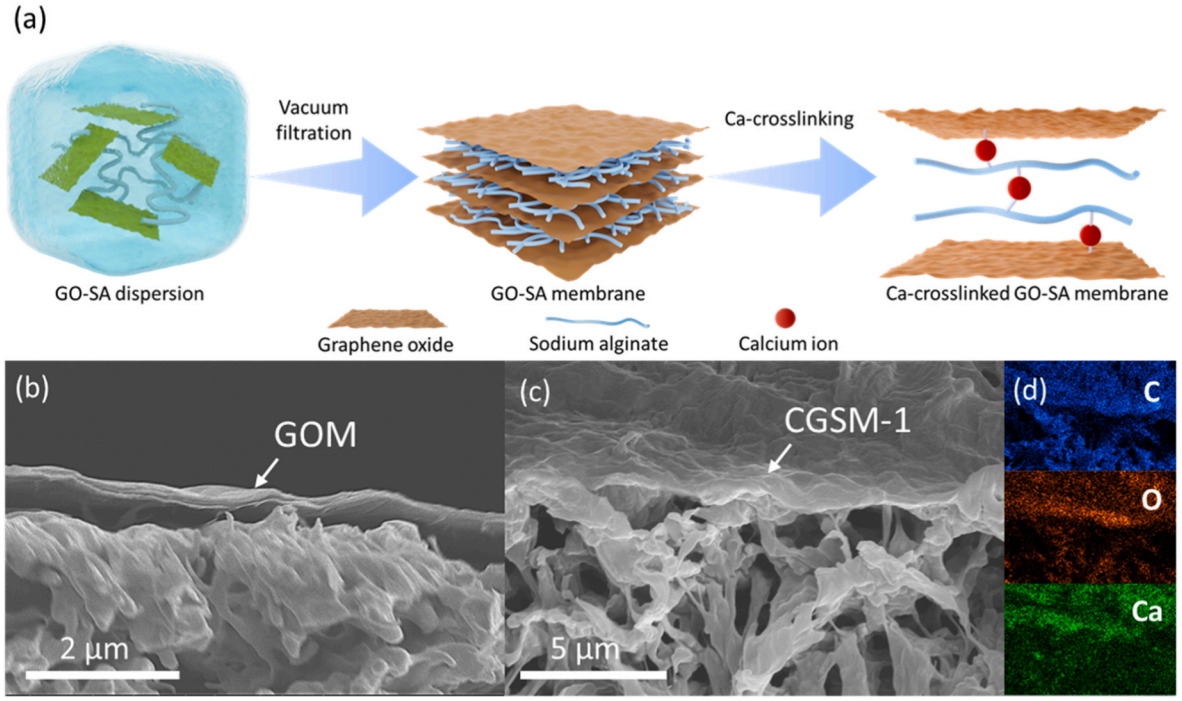

Fig. 2. (a) Schematic illustration showing the synthesis process of Ca^{2+}-crosslinked sodium alginate-intercalated graphene oxide membranes. **(b-c)** Cross-sectional scanning electron microscope (SEM) images of GOM (**b**) and CGSM-1 (**c**) showing the membrane morphology **(d)** Energy dispersive spectroscopy (EDS) elemental images based on (**c**) of carbon, oxygen and calcium.

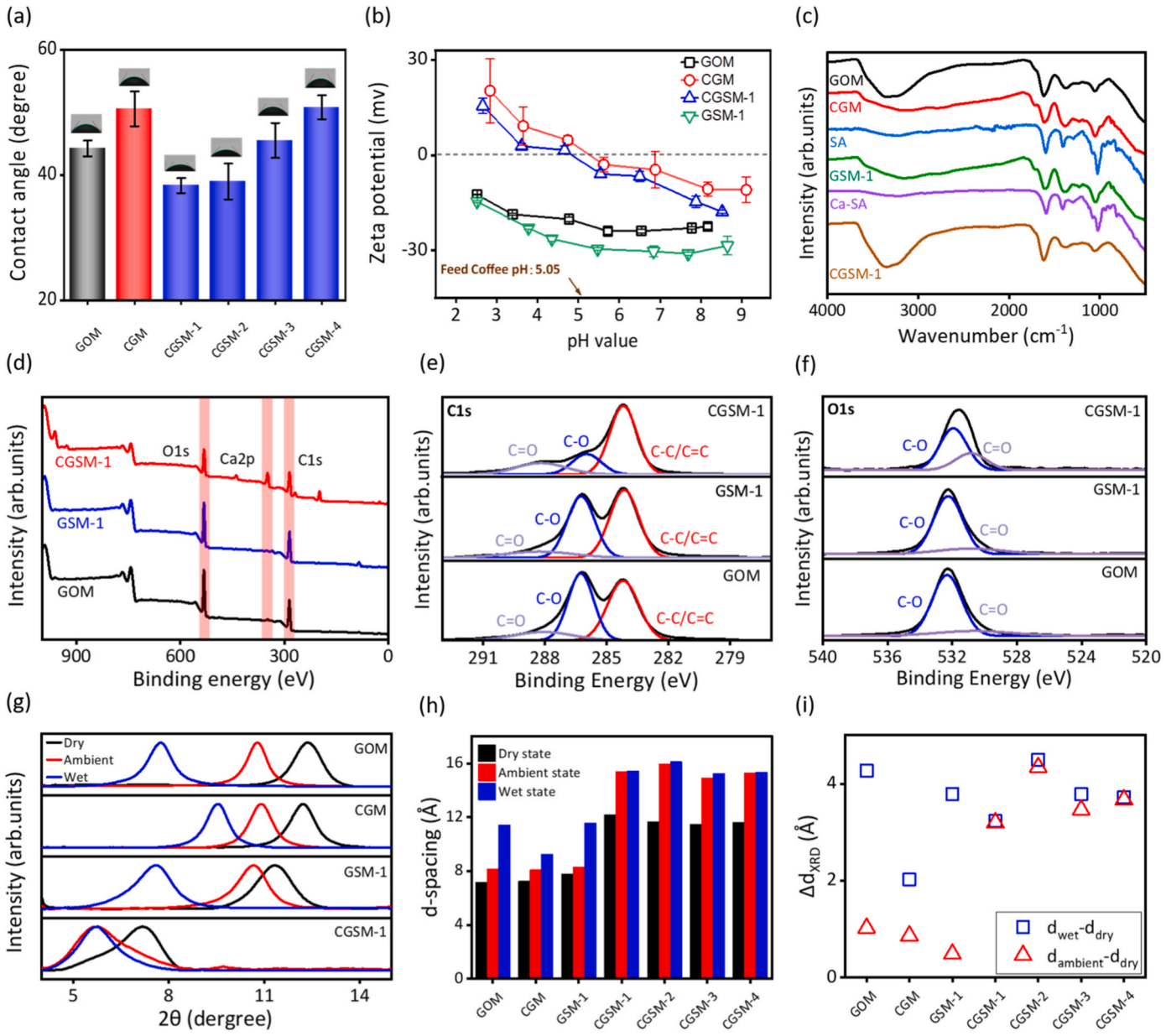

Fig. 3. Chemical composition and material structure characterizations of the membranes. **(a)** Contact angle measurements of GOM, CGM and CGSM membranes. **(b)** Surface zetapotential of GOM, CGM, CGSM and GSM membranes in the pH range of 2-9. **(c)** FT-IR spectra of GOM, CGM, SA GSM, Ca-SA and CGSM membranes. **(d-f)** XPS wide survey (**d**) with high resolution C1s (**e**) and O1s (**f**) spectra of GOM, GSM-1, CGSM-1. **(g)** XRD patterns of GOM, CGM, GSM and CGSM membranes in dry, ambient and wet states. **(h)** The d-spacing values of GOM, CGM, GSM, and CGSM membranes in dry, ambient, and wet states. **(i)** The d-spacing difference of GOM, CGM, and CGSM membranes between the ambient/wet state and the dry state.

and anchor the SA polymer chains onto the GO nanosheets. The high hydrophilicity of SA-Ca dominates the membrane properties, giving contact angles lower than that of GOM. For CGSM-3 and CGSM-4, as the SA content further increases, a dense network forms during Ca-crosslinking. This highly cross-linked structure not only encapsulates the GO nanosheets but also creates additional nanoscale wrinkles on the membrane surface. As a result, the contact angles become higher than that of GOM, which is consistent with the SEM observations.

The surface charge of the membranes was determined by solid-surface zeta potential measurements via streaming potential over the pH range 2.5 to 9, as shown in Fig. 3b. GOM and GSM-1 exhibit a negatively charged surface due to their abundant oxygen functional groups, and the deprotonation of oxygen functional groups under basic conditions leads to more negative zeta potentials [36]. For CGM and CGSM-1, upon the introduction of Ca^{2+} ions, the zeta potential becomes more positive; at pH below 5, both membranes exhibit positive zeta potentials.

The chemical composition of the samples and the crosslinking process were analyzed via FTIR, as shown in Fig. 3c and discussed in **Supplementary Note 5**. A typical broad GOM peak is observed at ~3375 cm^{-1}, originating from hydroxyl groups and adsorbed water [37]. With the introduction of Ca ions (CGM) and SA (GSM-1), this peak weakens, reflecting the disruption of the original hydration state of GOM and reducing the free water in the membranes. Another observation is that after Ca-crosslinking (Ca-SA), the 3375 cm^{-1} SA peaks decrease, indicating that Ca-crosslinking results in a more compact polymer matrix structure and therefore limits free water in the matrix. Compared with the other samples, CGSM-1 exhibits a deep, broad absorbance peak. This provides important evidence that, in the Ca-SA-GO ternary system, GO and SA are not isolated from each other; instead, they form an

enhanced intermolecular hydrogen-bonding network throughout the system due to Ca-crosslinking.

The enhanced hydrogen-bonding network in CGSM-1 is further supported by a strong FTIR absorption peak at approximately 3190 cm^{-1}. This peak is associated with O–H stretching vibrations [38]. According to the harmonic oscillator model derived from Hooke's law [39], the stretching wavenumber is directly related to the force constant of the vibrating bond:

$\tilde{\nu} = \frac{1}{2\pi c}\sqrt{\frac{k}{m}}$ where $\tilde{\nu}$ is the wavenumber, k is the bond force constant, m is the reduced mass, and c is the speed of light. Since the reduced mass remains essentially unchanged for O–H vibrations, any shift in wavenumber mainly reflects a change in the effective force constant of the O–H bond.

Stronger hydrogen bonding partially weakens and elongates the O–H covalent bond. This reduces the effective force constant of the O–H vibration, shifting the stretching band to a lower wavenumber. Therefore, the prominent peak at 3190 cm^{-1} indicates stronger hydrogen-bonding interactions and supports the formation of an enhanced hydrogen-bonding network in CGSM-1.

In the 1800–1200 cm^{-1} region, the peak near 1720 cm^{-1} is assigned to the C═O stretching vibration of protonated carboxyl groups [40]. This peak is observed in GOM, CGM and GSM-1, but becomes absent or strongly weakened in SA, Ca-SA and CGSM-1. This suggests that the carboxyl groups in the GO–SA system are mainly present as carboxylate species after SA intercalation and Ca^{2+} crosslinking. The peaks near 1600 and 1415 cm^{-1} are attributed to asymmetric and symmetric COO^{-} stretching vibrations, respectively [41–43]. The shifts of these bands after Ca^{2+} treatment support coordination between Ca^{2+} ions and carboxylate groups, confirming the formation of Ca^{2+}-mediated carboxylate interactions in the alginate-containing membranes.

In the fingerprint region, the peak around 1060 cm^{-1} is associated with C–O-related groups in GO-containing samples [37], while the sharp peak around 1025 cm^{-1} arises from C–O–C and C–O vibrations of the SA backbone [44]. After Ca^{2+} crosslinking, changes in these bands indicate that the local conformation of alginate chains and the oxygen-containing environment of GO are altered. In CGSM-1, the GO-related and SA-related C–O bands merge into a broader feature, suggesting a more complex local chemical environment within the GO–SA–Ca^{2+} nanochannels. Taken together, the FTIR results suggest that SA intercalation and Ca^{2+} crosslinking change the local chemical environment of the GO-based membranes. The changes in carboxylate-related bands support Ca^{2+} coordination with carboxyl groups, while the broad O–H region indicates possible changes in hydrogen-bonding environments. However, FTIR alone cannot directly confirm a fully integrated Ca–SA–GO network.

XPS was further used to analyse the surface chemical states of GOM, GSM-1 and CGSM-1 (Fig. 3d–f). The wide survey spectra (Fig. 3d) show the main C1s and O1s signals for all GO-based membranes, while the Ca2p signal appears in CGSM-1, confirming the successful introduction of Ca^{2+} after crosslinking. The high-resolution C1s spectra (Fig. 3e) can be deconvoluted into C–C/C═C, C–O and C═O components, corresponding to the graphitic carbon framework and oxygen-containing groups of GO and SA [45]. Compared with GOM and GSM-1, CGSM-1 shows lower relative C–O and C═O contributions. This decrease should not be interpreted as direct cleavage or loss of oxygen-containing groups. Instead, it suggests that these oxygen-containing groups may involve in new chemical environments after SA intercalation and Ca^{2+} crosslinking [46]. The lower C═O contribution is consistent with deprotonation and Ca^{2+} coordination of carboxyl groups, while the lower C–O contribution may be related to hydrogen bonding, Ca^{2+} coordination, or partial shielding by the crosslinked SA–Ca network. The O1s spectra (Fig. 3f) show a similar change in oxygen-containing components, further supporting the redistribution of oxygen chemical states in CGSM-1. Therefore, the XPS results support the FTIR interpretation that SA intercalation and Ca^{2+} crosslinking modify the local oxygen-containing chemical environment of the GO–SA system, rather than independently proving a complete Ca–SA–GO network.

Since FTIR and XPS mainly reflect local chemical environments, XRD was further used to examine whether these chemical changes are accompanied by changes in interlayer spacing, hydration behaviour and swelling stability. Fig. 3g shows the XRD patterns of GOM, CGM, GSM-1 and CGSM-1 in the dry, ambient and wet states, with the corresponding d-spacing values summarized in Fig. 3h. The diffraction peak reflects the average interlayer spacing of the laminar GO nanochannels [47]; therefore, a shift to a lower 2θ value indicates an increase in d-spacing. In the dry state, pristine GOM exhibits a characteristic GO diffraction peak at approximately 12.4°, corresponding to a d-spacing of 7.15 Å. After Ca^{2+} crosslinking, CGM shows only a slight change in dry-state d-spacing, indicating that Ca^{2+} mainly coordinates with oxygen-containing groups rather than strongly expanding the GO laminate. In contrast, introducing sodium alginate, especially after Ca^{2+} crosslinking, leads to a much larger interlayer spacing in the CGSM series, confirming that the Ca–SA network is successfully intercalated into the GO nanochannels. This is also confirmed by the XRD patterns of other CGSM membranes, as shown in **Supplementary Note 6** (Fig. S5).

The swelling behaviour under different hydration states further reveals structural difference between these membranes. For GOM, the diffraction peak shifts progressively to lower 2θ values from the dry state to the ambient state and further to the wet state, showing continuous water-induced swelling of the GO interlayer channels [48,49]. GSM-1 shows a similar trend, indicating that the introduction of SA alone improves hydrophilicity but does not effectively suppress swelling in water. By comparison, the CGSM membranes show different behaviour: their d-spacing increases significantly from the dry to the ambient state, but changes only slightly from the ambient to the wet state. This trend is more clearly shown in Fig. 3i, where the difference between $d_{wet} - d_{dry}$ and $d_{ambient} - d_{dry}$ is small for the CGSM series. This indicates that the CGSM membranes readily absorb water under ambient humidity and rapidly approach a hydrated, or hygroscopic, saturation state; however, once hydrated, their interlayer spacing remains relatively stable even under wet conditions [50].

In addition, the broader diffraction peaks of CGSM-1 indicate a wider distribution of interlayer spacings and reduced long-range order in the laminar structure [51,52]. This suggests that the Ca–SA network does not simply expand the GO layers uniformly but introduces a more heterogeneous interlayer architecture. Therefore, the XRD results demonstrate that Ca^{2+}-crosslinked SA intercalation simultaneously increases hydrated nanochannel size, enhances water affinity, and suppresses further wet-state swelling. Combined with the FTIR results, this suggests that the CGSM membranes possess locally stabilised Ca–SA–GO interactions while maintaining a more heterogeneous laminar stacking structure at the long-range scale.

Overall, the low water contact angle, the positive zeta potential at pH < 5, and the changes in d-spacing upon entering the wet state in the XRD data fully demonstrate that CGS exhibit a hydrophilic, positively charged surface, hygroscopic saturation, and anti-swelling properties. At the same time, FTIR results show that calcium ions improve the order of the local chemical environment through coordination with carboxyl groups, but the increase in XRD peak FWHM indicates that the long-range ordering of the layered structure is reduced. It can be recognised that the structure of CGS exhibits the coexistence of a locally ordered structure and an overall layered, disordered stacking.

3.3. Flat membrane decaffeination evaluations

The decaffeination performance of membranes was evaluated using a vacuum filtration apparatus at ~0.9 bar with 100 mL of coffee brew feed (1 mg/mL) for 24 h. The relevant performance indicators include caffeine removal (*Rem*), water permeance (*J*), concentration increase (*ΔC*), flavour-related marker retention index (*FRI*), and choline retention

(R_{cho}), as detailed in **Supplementary Note 7.** Freeze-drying did not alter the composition of the evaluation index, as verified in Table S3 (**Supplementary Note 8**).

We first evaluated the membrane selectivity and permeability. Five representative compounds in coffee with various molecular weights were selected for measurement (Fig. 4a), including n-methylpyridinium (NMP, 94.1 Da), choline (Cho, 104.2 Da), 5-hydroxymethylfurfural (HMF, 126.1 Da), trigonelline (Trig, 137.1 Da), and caffeine (Caf, 194.2 Da). Herein, Trig is an alkaloid and important coffee flavour precursor that undergoes degradation during roasting [53]. NMP is a characteristic roasting product formed from trigonelline degradation [32,54], and 5-HMF is a chemical marker commonly used to reflect roasting-induced chemical changes in coffee and other foods [53,55,56]. Generally, across all the GO-based membranes, choline has the highest rejection rate, while caffeine has the lowest. Notably, although caffeine has the largest molecular weight, its rejection rate is the lowest. This result indicates that membrane selectivity is not controlled by size exclusion alone. In nanofiltration, solute rejection can be influenced by coupled steric effects, Donnan exclusion, dielectric exclusion, membrane charge, hydration state and solute–membrane affinity [57–59]. In the present GO–SA–Ca^{2+} nanochannels, choline has a smaller molecular weight than caffeine, but it is permanently charged and highly hydrophilic. Therefore, it can interact more strongly with GO oxygen groups, alginate chains and Ca^{2+}-related hydrated sites through electrostatic interaction, hydration interaction and hydrogen bonding, leading to higher retention. In contrast, caffeine is larger but less ionised under the present aqueous condition, so it is less strongly retained by charge-related interactions. Although caffeine may interact with graphitic GO domains through π–π interaction and hydrogen bonding, these interactions can be dynamic and may allow adsorption–desorption-assisted transport through hydrated nanochannels [60,61]. Therefore, the preferential permeation of caffeine is attributed to the combined effects of molecular confinement, molecular charge, hydration state, surface affinity and confined transport, rather than molecular size alone.

Based on this coupled transport mechanism, CGSM-1 was further selected to examine whether its low caffeine rejection can translate into effective caffeine reduction in the retained coffee product while maintaining key non-caffeine compounds. The concentrations of representative coffee compounds in the original coffee, CGSM-1-treated coffee, and commercial decaf coffee were measured using quantitative nuclear magnetic resonance (qNMR) [28–32]. The results are summarized in Table 1. Different from conventional NF processes, where the permeate is usually collected as the purified product, the desired product in this work is the retained feed solution: caffeine preferentially permeates through the CGSM-1 membrane, while the main coffee matrix compounds are retained in the feed, thereby producing a decaffeinated coffee solution. Compared with the original coffee, the CGSM-1-treated coffee shows a clear reduction in caffeine concentration from 24.64 to 12.95 μg/mg, confirming its decaffeination ability. Importantly, the main coffee matrix compounds, including HMF, trigonelline, NMP and choline, are still retained at measurable levels, indicating that CGSM-1 can reduce caffeine while maintaining key non-caffeine compounds in the coffee matrix. Compared with the original coffee, commercial decaf coffee shows a substantially lower caffeine concentration, while some key non-caffeine compounds remain at relatively high levels. This may be related to differences in coffee source and processing conditions and may also reflect the possible addition or adjustment of flavour-related compounds after industrial decaffeination.

The water permeance was also monitored during the filtration process (Fig. 4b). Compared with pure GOM, introducing Ca ions (CGM) lowers the water permeance. Intercalating hydrophilic SA polymer

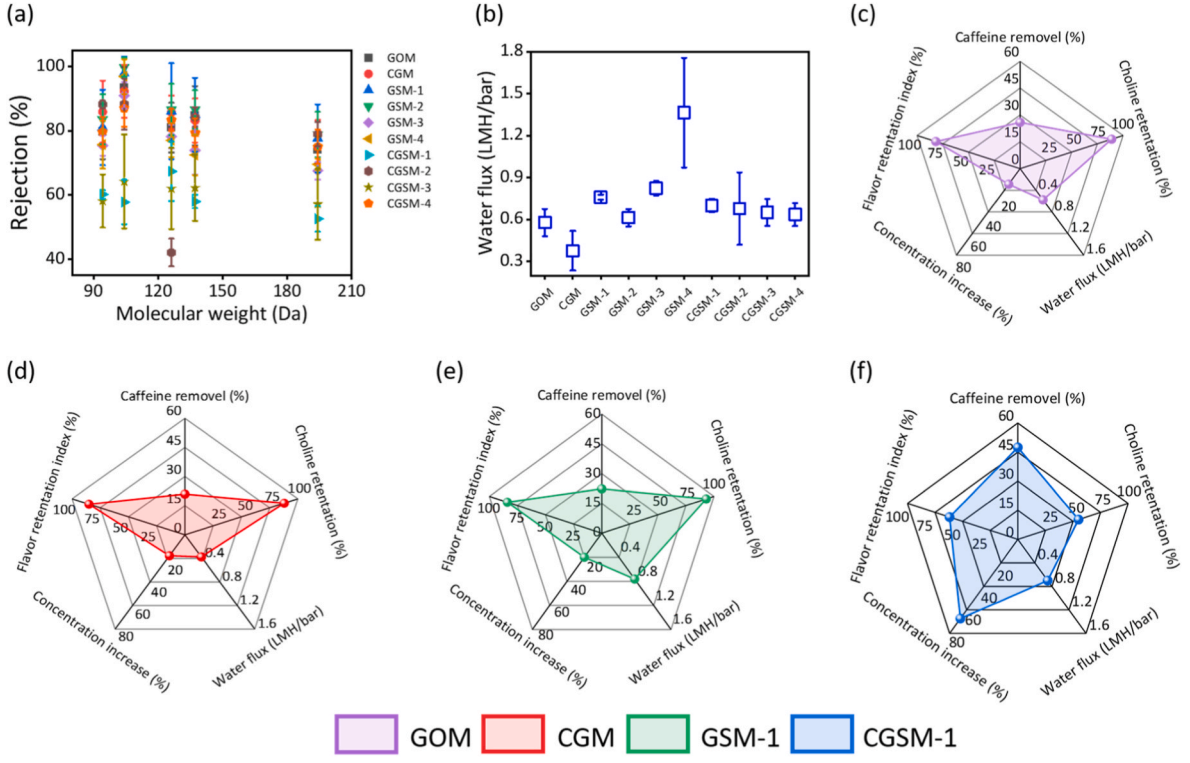

Fig. 4. Decaffeination performance of various membranes with 100 ml of coffee brew feed (1 mg/ml) for 24 h. **(a)** Rejection rate of five representative compounds in coffee of various synthesized membranes. The representative compounds with different molecular weight include n-methylpyridinium (NMP, 94.1 Da), choline (Cho, 104.2 Da), 5-hydroxymethylfurfural (HMF, 126.1 Da), trigonelline (Trig, 137.1 Da) and caffeine (Caf, 194.2 Da). **(b)** Water permeance of various synthesized membranes. The error bars indicate the standard deviation of three repeated measurements. **(c-f)** The performance evaluation in radar map of five criterions of various membranes including GOM (**c**), CGM (**d**), GSM-1 (**e**), and CGSM-1 (**f**). The five criterions include Caffeine removal (*Rem*, unit in %), Flavour-related marker retention index (*FRI*, unit in %), choline retention (R_{Cho}, unit in %), Water permeance (*J*, unit in LMH/bar) and concentration increase (ΔC, unit in %).

Table 1
Mean concentration of coffee compounds (M) and corresponding standard deviations (SD) of original coffee, CGSM-1 filtrated coffee and commercial decaf-coffee.

Sample name	Coffee compounds (μg/mg of freeze-dried coffee powder)									
	Caf		HMF		Trig		NMP		Cho	
	M	SD	M	SD	M	SD	M	SD	M	SD
Original coffee	24.64	0.66	1.85	0.04	3.21	0.08	1.29	0.05	0.85	0.01
CGSM-1	12.95	0.98	1.11	0.15	1.86	0.07	0.81	0.02	0.48	0.06
Decaf-coffee	0.52	0.03	0.48	0.01	3.52	0.02	0.66	0.01	0.70	0.03

chains significantly increases the water permeance, and GSM-4, with the highest SA intercalation, exhibits the highest water permeance of 1.36 LMH/bar. After Ca-crosslinking, CGSMs show a water permeance of around 0.6 to 0.7 LMH/bar, with a slight decrease as the SA intercalation amount increases. Comparing GSMs with CGSMs, Ca-crosslinking stabilises the membrane structure, resulting in less fluctuation in water permeance, but the highly crosslinked structure also leads to a lower water permeance. It should be noted that these values are apparent permeance measured during real coffee filtration, not intrinsic pure-water permeance. The modest permeance is likely caused by the combined resistance of the PVDF support, GO-based selective layer, compact Ca–SA–GO structure, and coffee-derived adsorption or fouling. Therefore, permeance is evaluated together with caffeine removal, flavour-marker retention, choline retention and concentration increase, rather than as the only performance criterion. To more comprehensively evaluate the decaffeination efficiency of the membranes, we distilled five parameters mentioned above and plotted radar maps (Fig. 4c–f). GOM, CGM and GSM-1 exhibit similar performance with high flavour and choline retention, while other indicators are relatively weak. However, the performance of CGSM-1 has changed significantly, emphasising improved caffeine removal and increased concentration while maintaining flavour, choline retention, and water permeance. The overall performance of CGSM-1 is more balanced, and the highest caffeine removal is more favourable for decaffeination.

In membrane-based decaffeination, the performance of the membranes cannot be assessed by a single indicator. Although the radar maps shown above can provide visualized evaluations, they are not sufficiently quantitative. Therefore, we established a multi-indicator evaluation framework (MCEF) combining the entropy weight method and the TOPSIS model to quantitatively and comprehensively compare the overall performance of different membranes [62,63]. We presented detailed data process methods in the multi-criteria performance evaluation section in **Supplementary Note 7**. Briefly, because the units of the performance indicators differ, we first normalise the indicators to eliminate the influence of units and value ranges and then determine the weight of each indicator using the entropy weight method. The idea of the entropy weight method is that if an indicator differs more significantly between membranes, it is better able to distinguish membrane performance and therefore should be given higher weight. It should be noted that the weights obtained by the entropy weight method is not assigned manually; rather, they are objectively calculated from the experimental data. After determining the weight for each indicator, the normalised data is multiplied by the corresponding weight to obtain a weighted normalisation matrix. Here, each indicator is not only normalised for evaluation in the same unit but also reflects its relative importance in the overall evaluation. The TOPSIS model is introduced to comprehensively rank the performance of the membranes. The principle of TOPSIS is that the optimal membrane should be as close as possible to the positive ideal membrane, while being as far as possible from the negative ideal membrane. Here, the positive ideal membrane is defined as the reference membrane with the highest value across all five indicators, whereas the negative ideal membrane is defined as the reference membrane with the lowest values across these indicators. The distances between each tested membrane and these two reference membranes are then calculated and used as the basis for the comprehensive performance ranking.

It should be noted that the MCEF used here is not limited to ranking the prepared membranes. In the present work, the positive and negative ideal solutions are generated from the experimental dataset to identify the best-performing membrane among the tested samples. However, the same framework can also be inverted for target-guided membrane design. For example, practical requirements such as a minimum caffeine removal, acceptable water permeance, flavour-related compound retention, and concentration increase can be defined first as target ranges. These targets can then be linked back to membrane properties, including interlayer spacing, surface charge, hydrophilicity, and swelling stability. Therefore, MCEF may provide not only a post-fabrication ranking method, but also a useful route for the a priori design of GO-based membranes for decaffeination and other complex separation processes.

The weighted normalisation matrix heatmap (Fig. 5a) demonstrates the contribution of each criterion to the overall evaluation. The detailed results are summarized in Table S4 (**Supplementary Note 9**). The weighted normalised values in the matrix are coupled by normalisation and weighting. The maximum value in each column represents the weight of the corresponding indicator [64]. Meanwhile, for a given column, the sample with the maximum value is the best-performing sample for that indicator. We first note that *Rem* and ΔC are assigned higher weights, since the evaluated membranes exhibit the greatest dispersion in these two performance indicators, and they will be significant in the performance ranking. On the other hand, *FRI* and R_{cho} have less weight and thus have less impact on the ranking. Here, we can easily figure out that CGSM-1 and CGSM-3 have the highest *Rem* and ΔC performance. Although they show relatively low performance on *FRI* and R_{cho}, they will still have a decisive advantage in the rankings.

We further developed a distance matrix (Fig. 5b) using **Euclidean** distances based on the weighted normalised values to perform a multi-dimensional similarity analysis to assess modification-performance relevance. In the distance matrix, a lower distance indicates higher similarity between two membranes across the five evaluation criteria, and the diagonal line shows that the distance between any membrane and itself is 0. The matrix can be divided into three groups. The first group consists of CGSM-1 and CGSM-3. These two samples demonstrate the highest *Rem* and ΔC performance, as shown above, and also exhibit high overall performance similarity. The second group includes GSM-3, GSM-4, and CGSM-4, with CGSM-4 having relatively independent performance characteristics. The third group comprises the remaining samples. We find that performance similarity is not strictly related to the modification, and different modification paths may achieve similar performance. This finding reveals that the influences of SA-intercalation and Ca-crosslinking on GOM are not monotonic, and multiple mechanisms may affect performance through coupling.

We performed the performance ranking using the TOPSIS model and calculated the closeness coefficient accordingly (Fig. 5c). CGSM-1 and CGSM-3 show the highest closeness coefficient, indicating their superior overall performance and their closeness to the ideal optimal membrane. Moreover, 60% of the samples show a higher closeness coefficient than that of GOM. The effectiveness of the modification strategy combining SA-intercalation and Ca-crosslinking for GOM can therefore be verified. However, we can also realize that modifying the membranes with

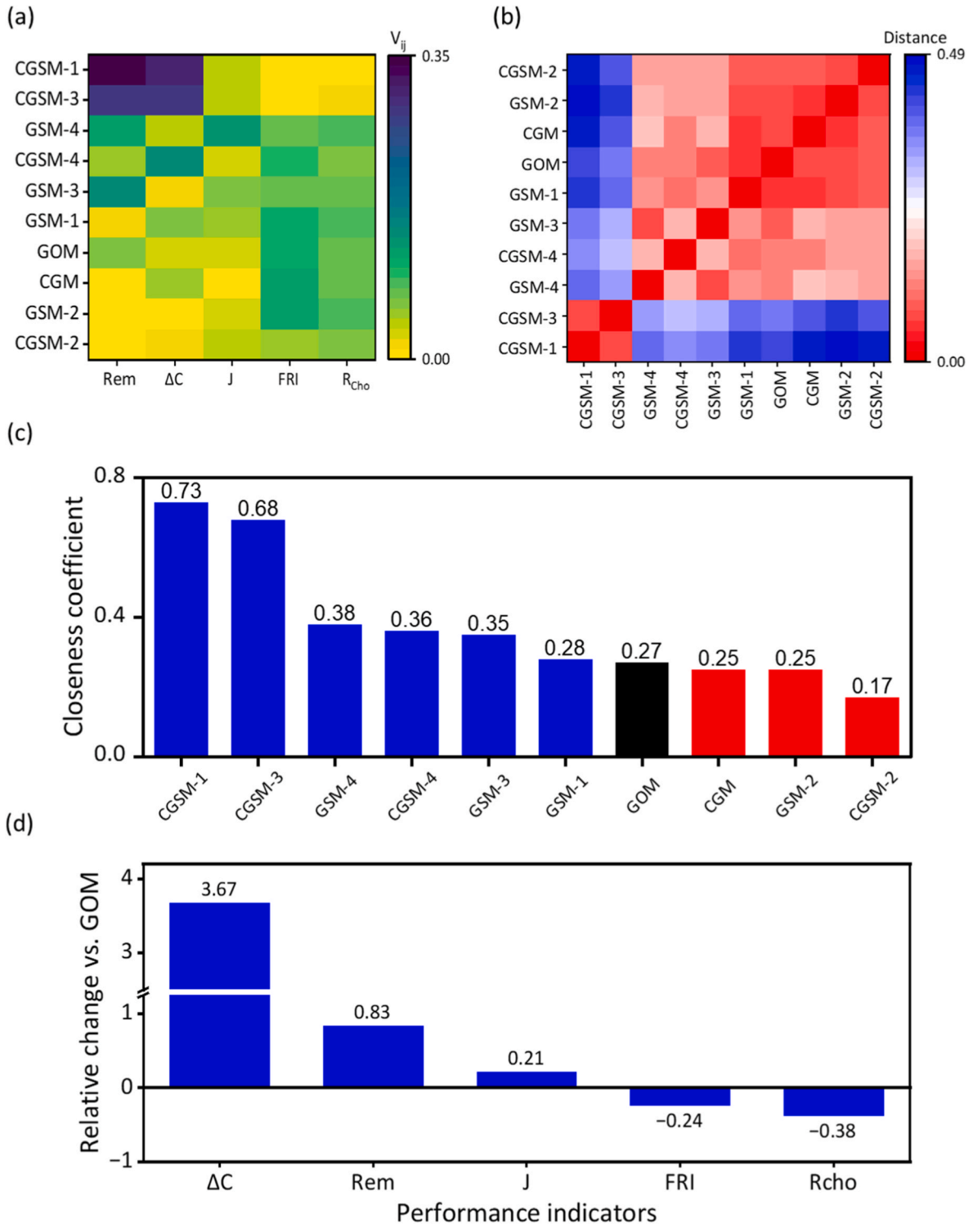

Fig. 5. (a) The entropy-weighted normalisation matrix heat map showing the contribution of five criterions to the overall evaluation of various membranes. Five criterions include Caffeine removal (*Rem*), Flavour-related marker retention index (*FRI)*, choline retention (R_{Cho}), Water permeance (*J*) and concentration increase (ΔC) are shown in the X axis of the matrix and various type of membranes are shown in the Y axis. **(b)** Euclidean distances matrix of various membranes across the five evaluation criterions. The high Euclidean distances are shown in blue and low distances are shown in red. **(c)** The bar chart of closeness coefficient presenting the overall performance of various membranes via TOPSIS model calculations. The blue bar chart indicates the membranes have a closeness coefficient larger than GOM, and the red bar chart shows one lower than GOM. **(d)** The relative closeness coefficient between CGSM-1 and GOM.

specific parameters does not necessarily improve their performance. For example, compared to GOM, CGM, GSM-2, and CGSM-2 have lower closeness coefficients and overall performance. Trade-offs among various performance indicators are always present in membrane evaluation, such that an increase in one property may lead to a decrease in one or more other properties. When considering a single indicator, we often overlook the decline in other indicators due to the trade-off effect. However, in practical applications, we often need a more balanced product. Therefore, it is necessary to evaluate the membranes, the effectiveness of the modifications, and their detailed parameters from a

more comprehensive perspective. Our established MCEF exhibits its superiority in the comprehensive evaluation of membrane performance. Compared to intuitive radar maps, the MCEF provides a more quantitative and objective model for converting multiple product selection criteria into a single straightforward coefficient that can assist in the quick and precise sieving of optimal membranes from a wide range of products [65].

With the assistance of MCEF, we determined that CGSM-1 is the optimal membrane for decaffeination in this work. We further compared CGSM-1 with GOM (Fig. 5d) to clarify performance contributions and assess the influence of modifications. CGSM-1 is superior to GOM in three indicators, ΔC, *Rem* and *J*, and this superiority is largely attributable to its significantly higher ΔC and *Rem*. Since a higher *Rem* represents lower caffeine rejection, CGSM-1 exhibits lower rejection rates for the five selected compounds than GOM, while achieving a higher concentration increase. This indicates that CGSM-1 has a sharper molecular sieving cut-off, which lowers the rejection of small molecules and increases the rejection of large molecules. As discussed in the membrane characterisation section, CGSM-1 has a larger interlayer spacing and a more neutral charge. Therefore, the increased *J* can be explained by the expanded nanochannels due to SA-intercalation [41,66]. Meanwhile, the introduction of Ca^{2+} shifts the membrane surface charge to a more positive or neutral state, which can weaken the Donnan exclusion effect for positively charged coffee compounds [67]. As discussed, SA intercalation and Ca^{2+} crosslinking introduces additional oxygen-containing and carboxylate-related sites, which may contribute to hydrogen bonding and adsorption interactions with polar coffee molecules. For caffeine, its aromatic structure may also interact with graphitic GO domains through π–π interactions [60,61]. Therefore, the improved caffeine removal and retained coffee matrix compounds in CGSM-1 are attributed to the coupled effects of enlarged hydrated nanochannels, tuned surface charge, molecular affinity, adsorption/desorption and confined transport [17,23]. To examine the scale-up potential of CGSM-1, we fabricated hollow fibre membranes and used GOM as a comparison.

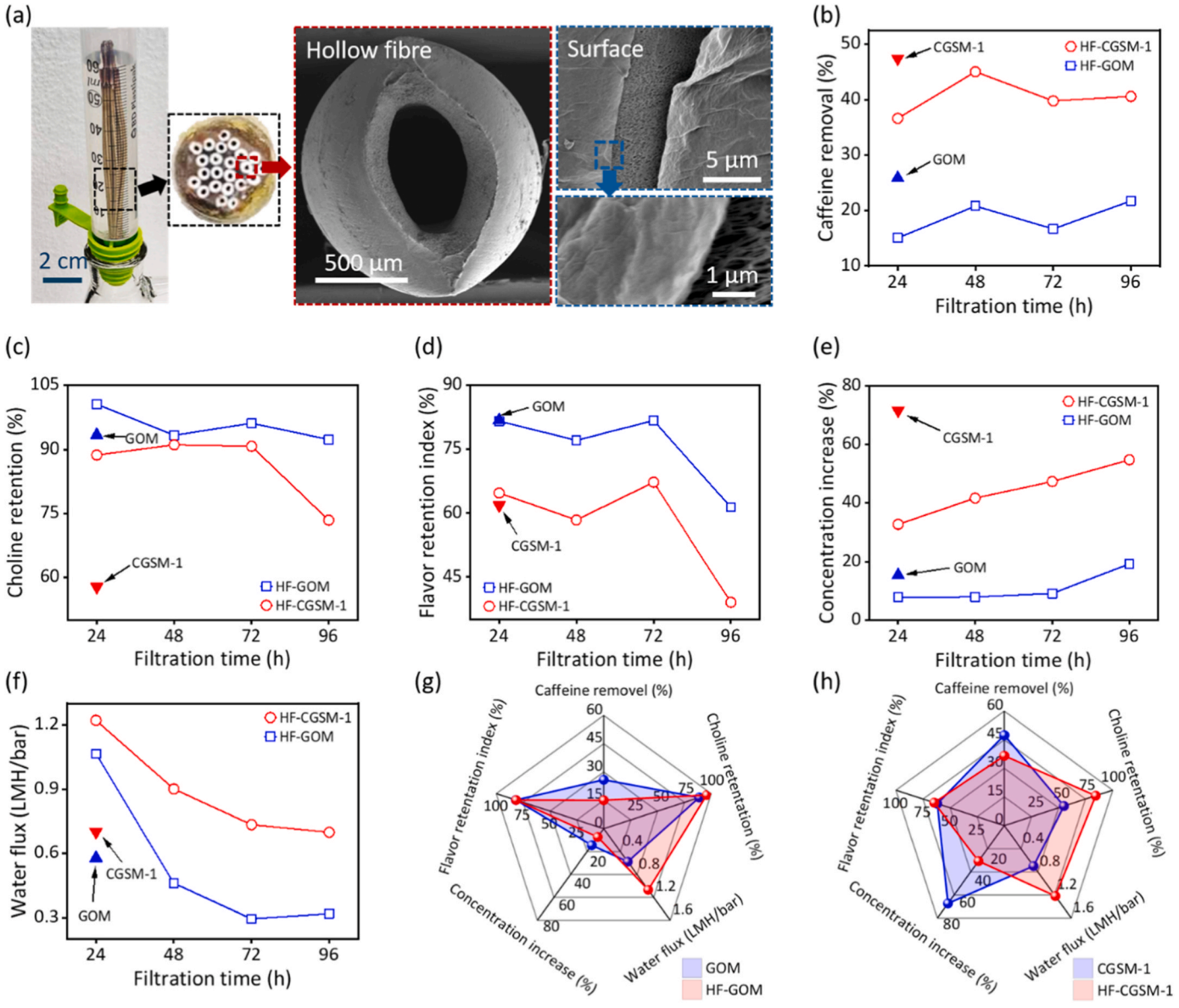

Fig. 6. (a) Digital photographs and scanning electron microscope (SEM) images of CGSA-coated GO-hollow fibre (HF) membranes (HF-CGSM-1) showing cross-section and in detail surface morphology. **(b-f)** The measured performance including caffeine removal (**b**), choline retention (**c**), flavour-related marker retention index (*FRI*) (**d**), concentration increase (**e**) and water permeance (**f**) of HF-CGSM-1. **(g-h)** The TOPSIS model calculated performances comparing GOM/HF-GOM (**g**) and CGSM/HF-CGSM-1 (**h**), indicating the differences between flat membranes and HF membranes.

3.4. Hollow fibre membrane filtration-based decaffeination

Hollow fibre (HF) membranes of GOM and CGSM-1 were fabricated via vacuum filtration [25], denoted as HF-GOM and HF-CGSM-1, respectively. During vacuum filtration, GO or GO–SA nanosheets are deposited onto the PVDF hollow-fibre surface to form a laminar selective coating. For HF-CGSM-1, SA intercalation and hydrogen bonding help organise the GO–SA layer, while Ca^{2+} crosslinking further stabilises the coating through carboxylate coordination. This combined deposition and crosslinking process helps maintain the modified nanochannel structure on the hollow-fibre support. The digital photos and SEM images of HF-CGSM-1 are shown in Fig. 6a, demonstrating a highly consistent morphology compared with CGSM-1. The HF membrane filtration-based decaffeination processes were carried out for 96 h with a sample interval of 24 h. We first compare performance over the first 24 h of operation between flat and HF membranes. During the first 24 h, the *Rem* and ΔC values of flat membranes are higher than those of HF membranes (Fig. 6b–e); in contrast, HF membranes exhibit higher Rcho and J values than flat membranes (Fig. 6c–f). For *FRI*, the values of HF membranes are close to those of flat membranes (Fig. 6d). We observe that, for both Rem and J, the performance difference between HF membranes and flat membranes remains at a similar level. On the other hand, for R_{cho} and ΔC, the difference between HF-CGSM-1 and CGSM-1 is larger than that between HF-GOM and GOM. The comprehensive comparison of the five selected indicators between HF membranes and flat membranes is shown in the radar maps (Fig. 6g for GOM and Fig. 6h for CGSM-1). We can intuitively see that the filtration behaviours between HF membranes and flat membranes are, to some extent, different [27,68], and the difference between HF-CGSM-1 and CGSM-1 is more significant. Compared with flat CGSM-1, HF-CGSM-1 more strongly highlights R_{cho} and *J*. The relatively higher *Rem* and R_{cho}, along with retained *FRI*, indicate that HF-CGSM-1 has a stronger rejection capability towards the five selected compounds than flat CGSM-1. The reduced ΔC can be attributed to enhanced adsorption of other coffee compounds on the membrane surface due to the increased membrane surface area. The comparison between HF membranes and flat membranes provides critical information that, for membranes with different chemical compositions and structures, the migration from flat membranes to HF membranes may not always achieve high consistency. Changes in macrostructure can also lead to changes in microstructure, thus altering filtration behaviours. Therefore, for membrane investigation and development aimed at industrial production, data obtained from flat membrane measurements cannot directly reflect their performance in HF membranes. Direct fabrication and performance evaluation of HF membranes are also essential.

The long-term (96 h) continuous operation examines the stability of the HF membranes. The *Rem* values of HF-CGSM-1 and HF-GOM fluctuate within the ranges 37%-45% and 15%-22%, respectively (Fig. 6b). Both the HF membranes exhibit relatively stable *Rem* performance over 96 h. For R_{cho} and *FRI*, the HF membranes experience a significant decrease from 72 h to the 96 h (Fig. 6c and d), except for the R_{cho} performance of HF-GOM. HF-CGSM-1 shows a continuous increase of ΔC (Fig. 6e). The ΔC of HF-GOM remains constant for the first 72 h and then increases between 72 h and 96 h. The J value of HF-CGSM-1 shows a continuous downward trend (Fig. 6f), with the decline slowing down between 72 h and 96 h. This permeance decline indicates that fouling occurred during long-term coffee filtration. This is reasonable because coffee is a complex organic mixture, and organic compounds may adsorb or deposit on the membrane surface and within near-surface nanochannels, thereby increasing transport resistance. This also confirms that the current hollow-fibre membrane is not yet optimised for high-throughput operation. The hollow-fibre result should therefore be viewed as an initial validation of geometry transferability and operating stability, rather than a fully optimised industrial module.

To further examine the membrane surface after operation, post-filtration SEM and EDS characterization were conducted for the best-performing CGSM-1 membrane, as shown in Fig. S6 (**Supplementary Note 10**). Compared with the pristine CGSM-1 surface, the used membrane shows surface deposits after coffee filtration. In addition, EDS analysis reveals the appearance of a nitrogen signal after filtration. Since the pristine membrane does not contain nitrogen as a major component, this nitrogen signal suggests the adsorption or deposition of nitrogen-containing coffee compounds on the membrane surface, providing direct evidence of organic fouling. On the other hand, the *J* value of GOM declines more sharply but shows a slight rebound between 72 h and 96 h. By combining the filtration performance data above, we can see that 72 h of continuous operation can lead to fouling of the HF membranes. Fouling can decrease both rejection rates and water permeance [69,70]. However, we observe that HF-CGSM-1 and HF-GOM exhibit similar filtration behaviours: both are fouled after long-term operation, but HF-CGSM-1 still outperforms HF-GOM. It should also be noted that a systematic cleaning and reuse study was not conducted in this work. Therefore, an optimum cleaning protocol cannot yet be proposed. Future work should evaluate mild hydraulic rinsing and weak alkaline cleaning strategies by comparing permeance recovery, caffeine-removal performance, retention of coffee matrix compounds, and membrane structural stability after repeated filtration–cleaning cycles. The superiority of HF-CGSM-1 not only confirms the effectiveness of the modification combining SA-intercalation and Ca-crosslinking but also demonstrates its robustness and scalability, as selected via our established MCEF.

To further place this membrane process in a practical context, representative industrial decaffeination methods are compared in Table S5 (**Supplementary note. 11**). Conventional organic solvent extraction, supercritical CO_2 extraction and Swiss Water-type processes mainly treat green coffee beans before roasting, and usually involve wetting or steaming, extraction, solvent or adsorbent management, and drying [2,3,71–73]. In contrast, the present GO-based membrane process directly treats instant-coffee aqueous solution at room temperature and low pressure, without adding organic extraction solvents during membrane treatment. This suggests its potential as a mild, water-based and modular route for liquid coffee streams. However, it is noted that this study remains at laboratory scale, which further work is required to evaluate permeance improvement, fouling control, cleaning, membrane lifetime, product recovery and process-level energy analysis.

4. Conclusion

This work demonstrates the potential of rationally modified GO-based membranes for membrane-based decaffeination, where caffeine removal, coffee compound retention, water permeance and membrane stability need to be balanced. In this study, SA intercalation, Ca^{2+} crosslinking and their combined modification were used to tune the GO nanochannel environment. The results show that these modifications do not lead to a simple monotonic improvement. Instead, the changes in interlayer spacing, surface chemistry, hydrophilicity, surface charge and swelling behaviour are coupled together, resulting in different trade-offs between permeance and selectivity.

To evaluate the membrane performance more comprehensively, five key indicators, including caffeine removal, flavour-related marker retention, choline retention, water permeance and concentration increase, were integrated into a multi-criteria evaluation framework combining entropy weighting and TOPSIS. Based on this framework, CGSM-1 was identified as the best-performing membrane among the tested GO-based membranes. This result shows that MCEF can provide a quantitative way to compare membranes with competing performance requirements and connect membrane modification with practical decaffeination performance.

Beyond ranking the prepared membranes, the MCEF may also provide a useful strategy for future target-guided membrane design. Practical targets, such as required caffeine removal, acceptable water permeance, flavour-related compound retention and concentration

increase, can be defined first and then linked back to membrane properties, including nanochannel size, surface charge, hydrophilicity and swelling stability. Therefore, the framework may be further developed from a post-fabrication evaluation method into a design tool for GO-based membranes in decaffeination and other complex liquid separations.

It should also be noted that this study is still an early-stage demonstration rather than an industrially optimised process. The present permeance remains modest under real-coffee filtration conditions. Further work is needed to improve permeance, reduce fouling, establish cleaning and reuse protocols, evaluate membrane lifetime, and assess process-level energy use and product recovery. Overall, this work identifies CGSM-1 as a promising membrane for selective caffeine reduction and highlights the value of multi-criteria evaluation for membrane systems with coupled structural changes and performance trade-offs.

CRediT authorship contribution statement

Yihan Tian: Conceptualization, Data curation, Formal analysis, Investigation, Methodology, Visualization, Writing – original draft. **Tongxi Lin:** Formal analysis, Methodology, Validation, Writing – review & editing. **Yuta Nishina:** Conceptualization, Supervision, Writing – review & editing. **Xiaojun Ren:** Formal analysis, Methodology, Supervision, Validation, Writing – review & editing. **Rakesh Joshi:** Conceptualization, Funding acquisition, Methodology, Project administration, Resources, Supervision, Writing – review & editing.

Declaration of competing interest

The authors declare the following financial interests/personal relationships which may be considered as potential competing interests: Rakesh Joshi reports financial support was provided by Australian Research Council Centre of Excellence for Carbon Science and Innovation. If there are other authors, they declare that they have no known competing financial interests or personal relationships that could have appeared to influence the work reported in this paper.

Acknowledgement

X.R. and R.J. acknowledge the funding support from the Australian Research Council, Centre of Excellence for Carbon Science and Innovation (CE230100032). The authors thank the staff of the Mark Wainwright Analytical Centre at UNSW for their technical assistance with sample characterization. The authors also acknowledge the use of ChatGPT 5 (OpenAI) exclusively for language editing. All scientific content, analysis, interpretation and conclusions are original.

Appendix A. Supplementary data

Supplementary data to this article can be found online at https://doi.org/10.1016/j.memsci.2026.125992.

Data availability

Data will be made available on request.

References

[1] A.S. Franca, Coffee: decaffeination, in: Encyclopedia of Food and Health, Elsevier, 2016, pp. 232–236, https://doi.org/10.1016/B978-0-12-384947-2.00183-5.
[2] D. Shofinita, D. Lestari, R. Purwadi, G.A. Sumampouw, K.C. Gunawan, S. A. Ambarwati, A.B. Achmadi, J.T. Tjahjadi, Effects of different decaffeination methods on caffeine contents, physicochemical, and sensory properties of coffee, Int. J. Food Eng. 20 (2024) 561–581, https://doi.org/10.1515/ijfe-2024-0013.
[3] Y.K. Ong, H.T. Ng, T.-S. Chung, A conceptual demonstration of decaffeination via nanofiltration, Ind. Eng. Chem. Res. 54 (2015) 7737–7742, https://doi.org/10.1021/acs.iecr.5b01737.
[4] C. Salgado, L. Palacio, F.J. Carmona, A. Hernández, P. Prádanos, Influence of low and high molecular weight compounds on the permeate flux decline in nanofiltration of red grape must, Desalination 315 (2013) 124–134, https://doi.org/10.1016/j.desal.2012.09.032.
[5] M. Catarino, A. Mendes, Dealcoholizing wine by membrane separation processes, Innov. Food Sci. Emerg. Technol. 12 (2011) 330–337, https://doi.org/10.1016/j.ifset.2011.03.006.
[6] S. Al-Ghamdi, B. Alfaifi, W. Elamin, M.A. Lateef, Advancements in coffee manufacturing: from dehydration techniques to quality control, Food Eng. Rev. 16 (2024) 513–539, https://doi.org/10.1007/s12393-024-09383-5.
[7] B. Nemzer, F. Al-Taher, N. Abshiru, E. de Mejia, Coffee and coffee By-Products as multifunctional foods and ingredients, Annu. Rev. Food Sci. Technol. 17 (2026) 133–154, https://doi.org/10.1146/annurev-food-052924-114847.
[8] A.I. Osman, Z. Chen, A.M. Elgarahy, M. Farghali, I.M.A. Mohamed, A.K. Priya, H. B. Hawash, P. Yap, Membrane technology for energy saving: principles, techniques, applications, challenges, and prospects, Adv. Energy Sustain. Res. 5 (2024), https://doi.org/10.1002/aesr.202400011.
[9] Y. Hiraga, C. Yoshida, K. Aoki, M. Watanabe, Efficient decaffeination of green coffee beans using pressure swing supercritical CO2 extraction, Innov. Food Sci. Emerg. Technol. 104 (2025) 104154, https://doi.org/10.1016/j.ifset.2025.104154.
[10] G. Basile, L. De Luca, G. Sorrentino, M. Calabrese, M. Esposito, F. Pizzolongo, R. Romano, Green technologies for extracting plant waste functional ingredients and new food formulation: a review, J. Food Sci. 89 (2024) 8156–8174, https://doi.org/10.1111/1750-3841.17487.
[11] T. Foller, R. Joshi, Let's discuss: when can we call a thin film 2-dimensional? Curr. Opin. Solid State Mater. Sci. 32 (2024) 101186 https://doi.org/10.1016/j.cossms.2024.101186.
[12] J. Abraham, K.S. Vasu, C.D. Williams, K. Gopinadhan, Y. Su, C.T. Cherian, J. Dix, E. Prestat, S.J. Haigh, I.V. Grigorieva, P. Carbone, A.K. Geim, R.R. Nair, Tunable sieving of ions using graphene oxide membranes, Nat. Nanotechnol. 12 (2017) 546–550, https://doi.org/10.1038/nnano.2017.21.
[13] H. Huang, Z. Song, N. Wei, L. Shi, Y. Mao, Y. Ying, L. Sun, Z. Xu, X. Peng, Ultrafast viscous water flow through nanostrand-channelled graphene oxide membranes, Nat. Commun. 4 (2013) 2979, https://doi.org/10.1038/ncomms3979.
[14] Y. Qian, J. Shang, D. Liu, G. Yang, X. Wang, C. Chen, L. Kou, W. Lei, Enhanced ion sieving of graphene oxide membranes via surface amine functionalization, J. Am. Chem. Soc. 143 (2021) 5080–5090, https://doi.org/10.1021/jacs.1c00575.
[15] S. Sibt-e-Hassan, K.A. Hasan, N. Adil, S.N. Khan, M. Usman, D. Hussain, S. G. Musharraf, Lysine-functionalized graphene oxide on cost-effective microporous support: a hydrophilic and fouling resistant membrane for safe lead filtration, Carbon N. Y. 223 (2024) 118974, https://doi.org/10.1016/j.carbon.2024.118974.
[16] P. Sun, H. Liu, K. Wang, M. Zhong, D. Wu, H. Zhu, Selective ion transport through functionalized graphene membranes based on delicate ion–graphene interactions, J. Phys. Chem. C 118 (2014) 19396–19401, https://doi.org/10.1021/jp504921p.
[17] T. Lin, X. Wen, X. Ren, V. Quintano, D.V. Andreeva, K.S. Novoselov, R. Joshi, Recent advances in graphene-based membranes with nanochannels and nanopores, Small Struct. 6 (2025), https://doi.org/10.1002/sstr.202400320.
[18] M. Hu, B. Mi, Enabling graphene oxide nanosheets as water separation membranes, Environ. Sci. Technol. 47 (2013) 3715–3723, https://doi.org/10.1021/es400571g.
[19] M. Zhang, Y. Mao, G. Liu, G. Liu, Y. Fan, W. Jin, Molecular bridges stabilize graphene oxide membranes in water, Angew. Chem. Int. Ed. 59 (2020) 1689–1695, https://doi.org/10.1002/anie.201913010.
[20] G. Zhao, H. Zhu, Self-regulating cross-linked graphene oxide membranes with stable retention properties over a wide pH range, Adv. Mater. Interfac. 7 (2020), https://doi.org/10.1002/admi.201901535.
[21] H.F.M. Austria, O. Setiawan, J. Widakdo, T.-H. Huang, T.M. Subrahmanya, W.-S. Hung, C.-C. Hu, K.-R. Lee, J.-Y. Lai, Investigation of the pH-mediated fabrication process of pure and polyethyleneimine-crosslinked graphene oxide membranes for desalination and heavy metal ion separation, Carbon N. Y. 224 (2024) 119019, https://doi.org/10.1016/j.carbon.2024.119019.
[22] G. Zhao, R. Hu, X. Zhao, Y. He, H. Zhu, High flux nanofiltration membranes prepared with a graphene oxide homo-structure, J. Memb. Sci. 585 (2019) 29–37, https://doi.org/10.1016/j.memsci.2019.05.028.
[23] X. Sui, Y. Wang, F. Liu, Z. Yuan, C. Wang, Y. Yu, K. Zhou, K. Goh, Y. Chen, The tripartite role of 2D covalent organic frameworks in graphene-based organic solvent nanofiltration membranes, Matter 4 (2021) 2953–2969, https://doi.org/10.1016/j.matt.2021.06.043.
[24] M. Zhang, K. Guan, J. Shen, G. Liu, Y. Fan, W. Jin, Nanoparticles@rGO membrane enabling highly enhanced water permeability and structural stability with preserved selectivity, AIChE J. 63 (2017) 5054–5063, https://doi.org/10.1002/aic.15939.
[25] H. Chen, T. Lin, M. Joshi, X. Ren, R. Joshi, Standard operating procedure for benchmarking and performance evaluation of graphene oxide membranes, Desalination 620 (2026) 119694, https://doi.org/10.1016/j.desal.2025.119694.
[26] X. Ren, D. Ji, X. Wen, H. Bustamante, R. Daiyan, T. Foller, Y.Y. Khine, R. Joshi, Graphene oxide membranes for effective removal of humic acid, J. Mater. Res. 37 (2022) 3362–3371, https://doi.org/10.1557/s43578-022-00647-6.
[27] T. Lin, Y. Wu, H. Chen, X. Ren, R. Joshi, Graphene oxide-polyvinyl alcohol nanofiltration membranes for efficient dye removal in practical conditions, J. Memb. Sci. 719 (2025) 123736, https://doi.org/10.1016/j.memsci.2025.123736.
[28] G.-L. Hu, C.-X. Quan, H.-P. Dai, M.-H. Qiu, Characterization of defective coffee beans and blends differentiation based on 1H qNMR technique, Curr. Res. Food Sci. 9 (2024) 100870, https://doi.org/10.1016/j.crfs.2024.100870.

[29] C. Ciaramelli, A. Palmioli, C. Airoldi, Coffee variety, origin and extraction procedure: implications for coffee beneficial effects on human health, Food Chem. 278 (2019) 47–55, https://doi.org/10.1016/j.foodchem.2018.11.063.
[30] G.F. Pauli, B.U. Jaki, D.C. Lankin, Quantitative ^{1}H NMR: development and potential of a method for natural products analysis, J. Nat. Prod. 68 (2005) 133–149, https://doi.org/10.1021/np0497301.
[31] G. del Campo, I. Berregi, R. Caracena, J. Zuriarrain, Quantitative determination of caffeine, formic acid, trigonelline and 5-(hydroxymethyl)furfural in soluble coffees by 1H NMR spectrometry, Talanta 81 (2010) 367–371, https://doi.org/10.1016/j.talanta.2009.12.010.
[32] N. D'Amelio, L. Fontanive, F. Uggeri, F. Suggi-Liverani, L. Navarini, NMR reinvestigation of the caffeine–chlorogenate complex in aqueous solution and in coffee brews, Food Biophys. 4 (2009) 321–330, https://doi.org/10.1007/s11483-009-9130-y.
[33] V. Saraswat, R.M. Jacobberger, J.S. Ostrander, C.L. Hummell, A.J. Way, J. Wang, M.T. Zanni, M.S. Arnold, Invariance of water permeance through size-differentiated graphene oxide laminates, ACS Nano 12 (2018) 7855–7865, https://doi.org/10.1021/acsnano.8b02015.
[34] J.-S. Yang, Y.-J. Xie, W. He, Research progress on chemical modification of alginate: a review, Carbohydr. Polym. 84 (2011) 33–39, https://doi.org/10.1016/j.carbpol.2010.11.048.
[35] S. Akshaya, A.J. Nathanael, A review on hydrophobically associated alginates: approaches and applications, ACS Omega 9 (2024) 4246–4262, https://doi.org/10.1021/acsomega.3c08619.
[36] M. Zhang, K. Guan, Y. Ji, G. Liu, W. Jin, N. Xu, Controllable ion transport by surface-charged graphene oxide membrane, Nat. Commun. 10 (2019) 1253, https://doi.org/10.1038/s41467-019-09286-8.
[37] Y. Si, E.T. Samulski, Synthesis of water soluble graphene, Nano Lett. 8 (2008) 1679–1682, https://doi.org/10.1021/nl080604h.
[38] J. Fan, Z. Shi, M. Lian, H. Li, J. Yin, Mechanically strong graphene oxide/sodium alginate/polyacrylamide nanocomposite hydrogel with improved dye adsorption capacity, J. Mater. Chem. A Mater 1 (2013) 7433, https://doi.org/10.1039/c3ta10639j.
[39] L.C. Wright, M.T. Oliver-Hoyo, Supporting the teaching of infrared spectroscopy concepts using a physical model, J. Chem. Educ. 96 (2019) 1015–1021, https://doi.org/10.1021/acs.jchemed.8b00805.
[40] B. Zhu, C. Guo, N. Li, P. Liu, M. Zhang, L. Wang, Z. Xu, From sheep track to motorway: supramolecular-mediated 2D nanofluidic channels for ultrafast water transport, Small 20 (2024), https://doi.org/10.1002/smll.202309253.
[41] J. Yu, Y. Wang, Y. He, Y. Gao, R. Hou, J. Ma, L. Zhang, X. Guo, L. Chen, Calcium ion-sodium alginate double cross-linked graphene oxide nanofiltration membrane with enhanced stability for efficient separation of dyes, Sep. Purif. Technol. 276 (2021) 119348, https://doi.org/10.1016/j.seppur.2021.119348.
[42] H. Zheng, J. Yang, S. Han, The synthesis and characteristics of sodium alginate/graphene oxide composite films crosslinked with multivalent cations, J. Appl. Polym. Sci. 133 (2016), https://doi.org/10.1002/app.43616.
[43] L. Wang, Y. Wang, J. Dai, S. Tian, A. Xie, X. Dai, J. Pan, Coordination-driven interfacial cross-linked graphene oxide-alginate nacre mesh with underwater superoleophobicity for oil-water separation, Carbohydr. Polym. 251 (2021) 117097, https://doi.org/10.1016/j.carbpol.2020.117097.
[44] A. Pragya, S. Mutalik, M.W. Younas, S.-K. Pang, P.-K. So, F. Wang, Z. Zheng, N. Noor, Dynamic cross-linking of an alginate–acrylamide tough hydrogel system: time-resolved *In situ* mapping of gel self-assembly, RSC Adv. 11 (2021) 10710–10726, https://doi.org/10.1039/D0RA09210J.
[45] I. Braccini, S. Pérez, Molecular basis of Ca^{2+} -Induced gelation in alginates and pectins: the egg-box model revisited, Biomacromolecules 2 (2001) 1089–1096, https://doi.org/10.1021/bm010008g.
[46] A. Kovtun, D. Jones, S. Dell'Elce, E. Treossi, A. Liscio, V. Palermo, Accurate chemical analysis of oxygenated graphene-based materials using X-ray photoelectron spectroscopy, Carbon N. Y. 143 (2019) 268–275, https://doi.org/10.1016/j.carbon.2018.11.012.
[47] X. Wen, T. Foller, X. Jin, T. Musso, P. Kumar, R. Joshi, Understanding water transport through graphene-based nanochannels via experimental control of slip length, Nat. Commun. 13 (2022) 5690, https://doi.org/10.1038/s41467-022-33456-w.
[48] R.R. Nair, H.A. Wu, P.N. Jayaram, I.V. Grigorieva, A.K. Geim, Unimpeded permeation of water through Helium-Leak–Tight graphene-based membranes, Science 335 (2012) 442–444, https://doi.org/10.1126/science.1211694, 1979.
[49] W. Liu, Y. Li, L. Xu, G. Wang, X. Ma, Y. Wang, Biomimic heterostructured graphene oxide membranes via supramolecular-mediated intercalation assembly for efficient water transport, Small 18 (2022), https://doi.org/10.1002/smll.202200461.
[50] F. Wang, Y. You, X. Jin, R. Joshi, On the role of driving force in water transport through nanochannels within graphene oxide laminates, Nanoscale 10 (2018) 21625–21628, https://doi.org/10.1039/C8NR08419J.
[51] A. Klechikov, J. Yu, D. Thomas, T. Sharifi, A.V. Talyzin, Structure of graphene oxide membranes in solvents and solutions, Nanoscale 7 (2015) 15374–15384, https://doi.org/10.1039/C5NR04096E.
[52] S. Zheng, Q. Tu, M. Wang, J.J. Urban, B. Mi, Correlating interlayer spacing and separation capability of graphene oxide membranes in organic solvents, ACS Nano 14 (2020) 6013–6023, https://doi.org/10.1021/acsnano.0c01550.
[53] J.-K. Moon, T. Shibamoto, Role of roasting conditions in the profile of volatile flavor chemicals formed from coffee beans, J. Agric. Food Chem. 57 (2009) 5823–5831, https://doi.org/10.1021/jf901136e.
[54] R. Lang, E.F. Yagar, A. Wahl, A. Beusch, A. Dunkel, N. Dieminger, R. Eggers, G. Bytof, H. Stiebitz, I. Lantz, T. Hofmann, Quantitative studies on roast kinetics for bioactives in coffee, J. Agric. Food Chem. 61 (2013) 12123–12128, https://doi.org/10.1021/jf403846g.
[55] F.C.O.L. Martins, G.M.R.N. Alcantara, A.F.S. Silva, W.R. Melchert, F.R.P. Rocha, The role of 5-hydroxymethylfurfural in food and recent advances in analytical methods, Food Chem. 395 (2022) 133539, https://doi.org/10.1016/j.foodchem.2022.133539.
[56] A. Hamzalıoğlu, V. Gökmen, 5-Hydroxymethylfurfural accumulation plays a critical role on acrylamide formation in coffee during roasting as confirmed by multiresponse kinetic modelling, Food Chem. 318 (2020) 126467, https://doi.org/10.1016/j.foodchem.2020.126467.
[57] C. Bellona, J.E. Drewes, The role of membrane surface charge and solute physico-chemical properties in the rejection of organic acids by NF membranes, J. Memb. Sci. 249 (2005) 227–234, https://doi.org/10.1016/j.memsci.2004.09.041.
[58] W.R. Bowen, J.S. Welfoot, Modelling the performance of membrane nanofiltration—critical assessment and model development, Chem. Eng. Sci. 57 (2002) 1121–1137, https://doi.org/10.1016/S0009-2509(01)00413-4.
[59] A. Yaroshchuk, Non-steric mechanisms of nanofiltration: superposition of Donnan and dielectric exclusion, Sep. Purif. Technol. 22–23 (2001) 143–158, https://doi.org/10.1016/S1383-5866(00)00159-3.
[60] J.A. Quintero-Jaramillo, J.I. Carrero-Mantilla, N.R. Sanabria-González, A review of caffeine adsorption studies onto various types of adsorbents, Sci. World J. 2021 (2021) 1–18, https://doi.org/10.1155/2021/9998924.
[61] A.R.D. Verliefde, E.R. Cornelissen, S.G.J. Heijman, E.M.V. Hoek, G.L. Amy, B. Van der Bruggen, J.C. van Dijk, Influence of Solute−Membrane affinity on rejection of uncharged organic solutes by nanofiltration membranes, Environ. Sci. Technol. 43 (2009) 2400–2406, https://doi.org/10.1021/es803146r.
[62] C.E. Shannon, A mathematical theory of communication, Bell Syst. Tech. J. 27 (1948) 379–423, https://doi.org/10.1002/j.1538-7305.1948.tb01338.x.
[63] C.L. Hwang, Kwangsun Yoon, Multiple Attribute Decision Making : Methods and Applications : a state-of-the-art Survey, Springer Verlag, 2012.
[64] P. Chen, Effects of the entropy weight on TOPSIS, Expert Syst. Appl. 168 (2021) 114186, https://doi.org/10.1016/j.eswa.2020.114186.
[65] M. Behzadian, S. Khanmohammadi Otaghsara, M. Yazdani, J. Ignatius, A state-of-the-art survey of TOPSIS applications, Expert Syst. Appl. 39 (2012) 13051–13069, https://doi.org/10.1016/j.eswa.2012.05.056.
[66] L. Yang, X. Xiao, S. Shen, J. Lama, M. Hu, F. Jia, Z. Han, H. Qu, L. Huang, Y. Wang, T. Wang, Z. Ye, Z. Zhu, J. Tang, J. Chen, Recent advances in graphene oxide membranes for nanofiltration, ACS Appl. Nano Mater. 5 (2022) 3121–3145, https://doi.org/10.1021/acsanm.1c04469.
[67] S.K. Tiwary, M. Singh, S.V. Chavan, A. Karim, Graphene oxide-based membranes for water desalination and purification, npj 2D Mater. Appl. 8 (2024) 27, https://doi.org/10.1038/s41699-024-00462-z.
[68] P. Yazgan-Birgi, M.I. Hassan Ali, H.A. Arafat, Comparative performance assessment of flat sheet and hollow fiber DCMD processes using CFD modeling, Sep. Purif. Technol. 212 (2019) 709–722, https://doi.org/10.1016/j.seppur.2018.11.085.
[69] T.K. Manios, A. Pihlajamäki, D. Mattia, M.R. Bird, Effect of fouling and cleaning upon the surface charge and porosity of polyethersulphone membranes during coffee brew decaffeination, Food Bioprod. Process. 141 (2023) 60–72, https://doi.org/10.1016/j.fbp.2023.07.005.
[70] T.K. Manios, D. Mattia, M.R. Bird, Fouling of polyethersulphone ultrafiltration membranes during the decaffeination of ground coffee brews, Food Bioprod. Process. 136 (2022) 14–23, https://doi.org/10.1016/j.fbp.2022.09.005.
[71] K. Ramalakshmi, B. Raghavan, Caffeine in coffee: its removal. Why and how? Crit. Rev. Food Sci. Nutr. 39 (1999) 441–456, https://doi.org/10.1080/10408699991279231.
[72] H. Peker, M.P. Srinivasan, J.M. Smith, B.J. McCoy, Caffeine extraction rates from coffee beans with supercritical carbon dioxide, AIChE J. 38 (1992) 761–770, https://doi.org/10.1002/aic.690380513.
[73] S. Saloko, Y. Sulastri, Murad, S. Wahyuni, The application of activated carbon from coconut shell and zeolite as adsorbents on coffee decaffeination using the Swiss Water process (SWP), IOP Conf. Ser. Earth Environ. Sci. 443 (2020) 012067, https://doi.org/10.1088/1755-1315/443/1/012067.